Synthesis of silver nanoparticles in green binary solvent for degradation of 2,4-D herbicide: Optimization and kinetic studies

N.S. Kamarudin[a], R. Jusoh[a,*], A.A. Jalil[b,c], H.D. Setiabudi[a], N.F. Sukor[a]

[a] Faculty of Chemical and Process Engineering Technology, Universiti Malaysia Pahang, 26300 Gambang Kuantan, Pahang, Malaysia
[b] Department of Chemical Engineering, Faculty of Chemical and Energy Engineering, Universiti Teknologi Malaysia, 81310 UTM Johor Bahru, Johor, Malaysia
[c] Centre of Hydrogen Energy, Institute of Future Energy, Universiti Teknologi Malaysia, 81310 UTM Johor Bahru, Johor, Malaysia

ARTICLE INFO

ABSTRACT

In this study, well-dispersed and diminutive Ag nanoparticles have been successfully synthesized in binary solvent of *Orthosiphon stamineus* (OS) leaves extract and ionic liquids (ILs) via electrochemical method. ILs namely [BMIM Tf$_2$N], [BMIM BF$_4$] and [EMIM EtSO$_4$] were used as solvent in the synthesis process to produce Ag$_{Tf2N}$, Ag$_{BF4}$, and Ag$_{EtSO4}$. The characterization of Ag nanoparticles revealed that the particle size of the silver nanoparticles can be easily altered depending on the size of IL alkyl chain and anion, to produce ultrafine particles ranging from 8 to 25 nm. Meanwhile, the photocatalytic activity of Ag$_{Tf2N}$ nanoparticles effectively degraded the highest amount of 2,4-dichlorophenoxyacetic acid (2,4-D) herbicide at 65.61%. The optimized model gave high removal percentage of 2,4-D at 97.80% (pH = 3.24; catalyst dosage = 0.009 g/L; 2,4-D concentration = 8.15 mg L^{-1}) with validation experiments of 1.28% error. Investigation of kinetic reaction showed the applicability of pseudo-first order kinetic to the process of 2,4-D degradation (R^2 > 0.98) which positively predicted the constant elimination amount of 2,4-D throughout the photocatalytic process. Overall, the studies construed the crucial role of binary solvent in synthesizing and controlling the size of Ag nanoparticles for pollutant degradation.

© 2020 Institution of Chemical Engineers. Published by Elsevier B.V. All rights reserved.

1. Introduction

Nowadays, herbicides especially 2,4-dichlorophenoxyacetic acid (2,4-D) have become one of the main pollutants in wastewater due to the persistently and heavily used for agriculture and industrial production (Liu et al., 2017). These herbicides were chemically stable and may penetrate deeply into the groundwater leading to the negative effect on human health and environment (Kadi et al., 2018). Therefore, these pollutants should be adequately treated before discharged to the environment. There are several methods that are frequently used to remove these pollutants including chemical oxidation, adsorption on activated carbon, coagulation, flocculation, activated sludge, and biodegradation (Jaafar et al., 2017). However, these methods are fraught with many problems, including time consumption and expensiveness. Therefore, photocatalytic degradation is regarded as one of the most competitive techniques for remedying environmental pollution (Xu et al., 2017). This method has been proved to be effective method to degrade organic pollutants in wastewater (Liu et al., 2016). Various photocatalysts have also been synthesized and widely applied in the photocatalytic degradation of organic contaminants (Jaafar et al., 2015; Lv et al., 2016; Zhang et al., 2015a,b). Among them, the noble metal such as

---

silver (Ag) has received immense research as a photocatalyst in the photocatalytic degradation (Hamedi et al., 2017; Kumar et al., 2013). This is due to the fact that Ag nanoparticles have a low band gap of ~2.2 eV which significantly important in a photocatalytic process (Ali et al., 2018).

There are various synthesis routes for Ag nanoparticles that can be used in attaining desired sizes, shape and functionalities, which include chemical reduction, photo reduction, the electrochemical method, atom beam sputtering, and radiation assisted method (Hareesh et al., 2016). Particularly, the electrochemical techniques have been widely employed due to the high purity of the particles and the probability in obtaining precise particle size (Bezares et al., 2015). Diverse selection of toxic chemicals has been used as solvents in the electrochemical cells which endangered human beings and environment. Green chemistry commands the minimization on toxic chemical substances application, but environmental safer solvents instead (Tzani et al., 2017). This present work demonstrated primarily green synthesis of Ag nanoparticles using aqueous *Orthosiphon stamineus* leaves extract along with different ionic liquids (ILs) as solvent. This effective green media was designed to synthesis nanoparticles via electrochemical method.

O. stamineus (OS) or commonly known as "Misai Kucing" (Cat's Whisker) belongs to Lamiaceae family and is extensively used as folklore Asian herbal medicine for the treatment of variety of diseases including inflammation, bacterial infections, urinary tract infections, influenza, rheumatism, jaundice, and angiogenesis-related problems like cancer (Yehya et al., 2019). OS has been reported to contain antioxidant, which can act as a reducing and capping agent for the Ag synthesis process. The leaves extract is a complex mixture which contains substantial amounts of phenolic compounds that has antioxidant effect such as rosmarinic acid, caffeic acid, sinensetin, eupatorin, also an undetermined quantity of other unknown constituents (Ariff et al., 2012). Past studies were also reported implementing this green synthesis method of Ag nanoparticles using different plants such as *Cassia auriculata* and *Sargassum Boveanum* that rich in phenolic compounds known for its antioxidant activity (Farrokhnia et al., 2017; Muthu and Priya, 2017). Both plants exhibited excellent performance for the catalytic reduction of methyl orange and 4-nitrophenol also in H_2O_2 detection.

On the other hand, the employment of ILs in synthesis process of metal nanoparticles has immerged to be a very good substitution for volatile organic compounds (VOCs) that are known to be toxic, volatile and flammable (González et al., 2018; Jafari et al., 2019). Besides, ILs are also considered as green solvents mainly due to their unique properties such as chemical and thermal stability, non-flammability, negligible vapour pressure, high synthetic flexibility, good dissolving ability, high ionic conductivity and nontoxicity (Ambika and Sundrarajan, 2016; Tshemese et al., 2018). In addition, ILs were reportedly to be more efficient to be used for higher extraction yields of these bioactive compounds (Irfan et al., 2017; Passos et al., 2014). In the recent years, ILs have been widely employed in the preparation of nanoparticles due to the abundance of ions that can be used as electrolytes in the electrochemical cell as well as the stabilizing and capping agent (Ambika and Sundrarajan, 2016; Khan et al., 2012; Passos et al., 2014). Past study by Tzani et al. (2017) obtained average silver nanoparticles size of 63–108 nm using different type of ionic liquids. The

study claimed that the ILs provide protective electrostatic shell that formed during the synthesis process to prevent oxidative degradation and agglomeration of the particles. Different type of ionic liquid generated different size of nanoparticles, hence it can be carefully stated that the type of ILs may altered the nanoparticles size. However, there are insufficient studies that emphasized the synergistic effect of binary solvent from plant extract and ILs as an aqueous media in the electrosynthesis for nanoparticles size alteration. Although study on the synthesis of silver nanoparticles using ILs as media has been widely discovered (Corrêa et al., 2016; Husanu et al., 2018). However, there are insufficient studies that emphasized the synergistic effect of binary solvent from plant extract and ILs as an aqueous media in the electrosynthesis for nanoparticles size alteration.

Previously, the one factor at a time (OFAT) method was used in the optimization of the operating parameter by varying one factor at a time while fixing the other factors (Fattahian et al., 2018). However, high numbers of experiments need to be done in obtaining the maximum result of each factor, aside being time consuming, expensive and less efficient. Response surface methodology (RSM), a highly efficient statistical tool has been extensively used to replace the traditional OFAT system to determine the optimum condition of the system and understand the factor–response relationship (Dehghani et al., 2017). In approximated a response function to experimental data, few experimental designs can be implements such as central composite design (CCD), Box–Behnken Design, One Factor Design, and 3-Level Factorial Design, which each of them promotes different characteristic and efficiency. Among them, CCD has been commonly applied in the study of photocatalytic degradation (Mirzaei et al., 2018; Priya et al., 2018). Despite extensive research on the implementation of RSM for photocatalytic degradation before, there are very limited studies on optimization degradation using binary solvents.

Currently, there are many researches that emphasized on the development of simple and green routes on the synthesis of nanoparticles (Hekmati et al., 2020; Patil et al., 2020; Singh et al., 2019). However, most of these studies only focuses on the use of either plant extract or ionic liquid as the synthesis media (Jayarambabu et al., 2020; Jini and Sharmila, 2019; Ravichandran et al., 2019). Moreover, there are very limited studies on the implementation of green solvent as an electrolyte for electrosynthesis process (Sapawe et al., 2019). According to author's knowledge, no work has been carried out on the utilization of binary solvent of plant extract and ILs in the electrosynthesis of nanoparticles, especially for size alteration. Therefore, it signifies the main novelty of this study in the preparation and stabilization of Ag nanoparticles using binary solvent (plant extract and IL) for electrosynthesis process. Hence, in this study, the role of different types of ILs (1-butyl-3-methylimidazolium bis (trifluoromethylsulfonyl) imide, [BMIM Tf$_2$N], 1-butyl-3-methylimidazolium tetrafluoroborate, [BMIM B$_F$4] and 1-ethyl-3-methylimidazolium ethyl sulfate), [EMIM EtSO$_4$] towards size alteration was investigated. The catalysts were characterized using X-ray diffraction, Fourier transform infrared spectroscopy, transmission electron microscopy and Brunauer–Emmett–Teller. Then, the optimum condition of 2,4-D degradation was optimized by response surface methodology (RSM). Finally, the kinetic analysis was investigated to reflect the catalytic degradation process of 2,4-D.

2. Experimental

2.1. Materials

OS leaves were collected from Jabatan Pertanian Negeri Pahang, Malaysia. Electrodes (silver and platinum plates) were attained from Nilaco, Japan 2,4-dicholorophenoxyacetic acid (2,4-D), while sodium hydroxide (NaOH) and hydrochloric acid (HCL) were purchased from Merck, Malaysia. Three types of ionic liquids (ILs) which are 1-butyl-3-methylimidazolium bis(trifluoromethylsulfonyl) imide [BMIM Tf$_2$N], 1-butyl-3-methylimidazolium tetrafluoroborate [BMIM BF$_4$], 1-ethyl-3-methylimidazolium ethyl sulfate [BMIM EtSO$_4$] were purchased from Nano Life Quest Sdn Bhd.

2.2. Preparation of OS leaves extraction and silver (Ag) nanoparticles

A finely crushed powder form of OS leaves was used in this experiment. 1.5 g of the powder was immersed into 100 mL of 0.1 M ILs solution. After boiling for 2 h at 60 °C, the powder was filtered leaving only the extract solution. The solution then was cooled before it was used as a media in the electrolysis process. The electrochemical cell which consists of a two-electrode system which is Ag plate as an anode and platinum plate as the cathode was used in this synthesis process (Jusoh et al., 2015a). Electrolysis process was carried out at a constant current of 480×10^{-3} A under the air atmosphere with the extraction sample was used as a media. Then, the solution product mixture was immersed in the water bath at 80 °C before dry overnight in an oven at 110 °C. The prepared Ag nanoparticles in [BMIM Tf$_2$N], [BMIM BF$_4$] and [BMIM EtSO$_4$] solution were denoted as Ag$_{Tf2N}$, Ag$_{BF4}$ and Ag$_{EtSO4}$, respectively. Meanwhile, the prepared Ag nanoparticle with the absence of ILs was denoted as Ag$_B$.

2.3. High performance liquid chromatography (HPLC) analysis of phenolic compounds

The measurements of separation and determination of phenolic compound; as gallic acid from the OS leaves were performed using an high performance liquid chromatography (HPLC) system Agilent Series 1100 equipped with diode array detection (DAD) and a column Phenomenex Prodigy 5 μ (250 mm × 4.60 mm). The wavelength for detection of gallic acid was set at 270 nm. Separation was achieved by flow rate of 1 mL/min with 3.0% phosphoric acid (90%)/acetonitrile (10%), in an isocratic programme. The injection volume was 10 μL. Each sample and standard was filtered with nylon syringe filter (pore size of 0.22 μm). In preparing for the standard curve, GA standard was prepared at concentration 10–60 ppm. The phenolic content was expressed as milligrams of gallic acid equivalents per kilograms of sample (mg GAE/kg sample).

2.4. Characterization of Ag nanoparticles

The crystallinity of the Ag nanoparticles was analyzed by X-ray powder diffraction (XRD) (D8 ADVANCE Bruker X-ray diffractometer) using CuKα radiation at a range of $2\theta = 0$–90°. The chemical components in the synthesized catalyst were identified by using Fourier transforms infrared (FTIR) spectra (Perkin Elmer Spectrum GX FTIR Spectrometer). The samples were characterized using the KBr pellet technique with a range of 400–4000 cm^{-1}. The morphology of the Ag nanoparticles was observed by Transmission electron microscopy (TEM) (JEOL JEM-2100F) and the specific surface area of the Ag nanoparticles values was calculated from the Brunauer–Emmett–Teller (BET) analysis.

2.5. Adsorption and photodegradation of 2,4-dichlorophenoxyacetic acid (2,4-D) herbicide

The photocatalytic activity of the Ag nanoparticles was then tested on the photodegradation of the 2,4-D). The photocatalytic experiments were performed in a Pyrex batch photoreactor, 140 mm length and 85 mm diameter with a total volume of 0.25 m^3. The photoreactor was also fixed with UV lamp and cooling system. The photocatalytic reactor set-up was displayed in Fig. S1. 5 mg L^{-1} stock solutions of 2,4-D was prepared by dissolving 0.25 mg of Ag nanoparticles in 500 mL of deionized water at pH 3. Then, the solution was added to a beaker before it was put in a batch photoreactor fixed with 39 W metal halide lamps (400 nm) and a cooling system. The suspension was stirred constantly for 30 min in dark condition to reach adsorption/desorption equilibrium. After adsorption, the mixed suspension was exposed under light irradiation for 180 min. At a regular interval of time, the sample was withdrawn and centrifuged at 5000 rpm for 15 min. The absorbance of the supernatant was then measured using a UV–visible spectrophotometer wavelength of 227 nm. The percentage removal could be calculated by using the following Eq. (1):

$$\text{Degradation}(\%) = \left(\frac{C_0 - C_t}{C_0} \right) \times 100 \tag{1}$$

where C_0 is the initial concentration of the 2,4-D solution and C_t is the concentration of solution after t hours of exposure in light sources. The experiment was repeated at different pH (2, 2.5, 3, 3.5, 4), catalyst dosage (0.005 g/L, 0.008 g/L, 0.01 g/L, 0.013 g/L and 0.015 g/L) and initial concentration (5 mg L^{-1}, 7.5 mg L^{-1}, 10 mg L^{-1}, 12.5 mg L^{-1} and 15 mg L^{-1}).

2.6. Experimental design and optimization

The central composite design (CCD) under response surface methodology (RSM) was used in determining the optimum conditions of 2,4-D degradation by varying the three independent factors including pH (2–4), catalyst dosage (0.005–0.015 g/L) and initial concentration of 2,4-D (5–15 mg L^{-1}). The independent variables and the real values of the coded level, high (+) and low (−) were tabulated in Table S1. In this study, the Design Expert software Version 7.1.6 was used for data analysis. The significance and adequacy of the developed regression model were justified by the analysis of variance (ANOVA).

3. Results and discussions

3.1. Identification of phenolic compound in the sample

In order to identify the presence of phenolic compound in the OS leaves extract, HPLC analysis was used to quantify the target compound present in the sample. Based on Fig. 1A, the samples extract yielded 33,605.73 mg GAE/kg of phenolic compound after boiling for 2 h. The phenolic compound from plant extract is capable to reduce silver ions (Ag$^+$) to zero-valent sil-
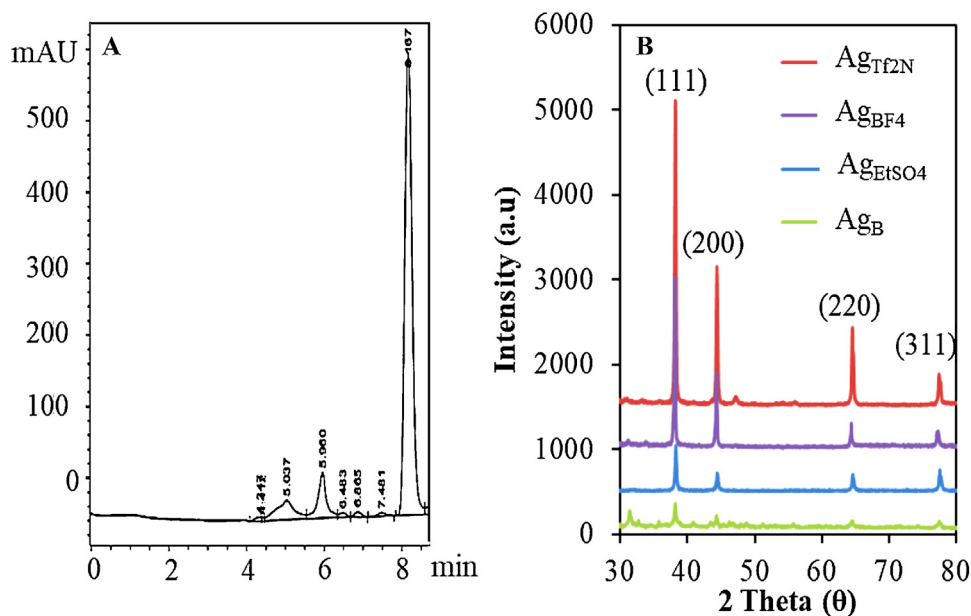
Fig. 1 – (A) Chromatograph of phenolic compound in OS leaves extract; (B) XRD patterns of Ag nanoparticles.

ver nanoparticles (Ag⁰) during synthesis process (Denrah and Sarkar, 2019). In addition, past reports claimed that the phenolic compounds have potential to bind metal ions to form nanoparticles (capping agent) and has the ability to encapsulate the Ag⁰ nanoparticles to prevent agglomeration and thereby give positive stabilization effect on the nanoparticle for further photocatalytic degradation process (Saeed et al., 2019a,b).

3.2. Characterization of Ag nanoparticles

3.2.1. X-ray diffraction analysis

The crystalline structures of Ag_B and IL-stabilized Ag_{Tf2N}, Ag_{BF4} and Ag_{EtSO4} nanoparticles were examined by XRD analysis (Fig. 1B). The diffraction peaks of Ag nanoparticles at 2θ values of 38.01°, 44.0°, 64.33° and 77.29°, correspond to (1 1 1), (2 0 0), (2 2 0) and (3 1 1) planes, respectively. The displayed Bragg reflection could be indexed to face-centred cubic crystal structure of bulk metallic Ag (JCPDS file no. 89-3722) (Verma et al., 2016). The (1 0 0) peak intensity of the prepared Ag without ILs (Ag_B) was seen reduced as compared with other (1 0 0) peak of the prepared Ag with the presence of ILs (Ag_{Tf2N}, Ag_{BF4}, Ag_{EtSO4}), signifying a less-ordered structural arrangement of the catalyst in Ag_B sample. This indicated the plausible involvement of the ILs in the structural arrangement of the catalyst (Jusoh et al., 2015a). In addition, no other peak was found in the XRD pattern of the Ag_{Tf2N}, Ag_{BF4}, and Ag_{EtSO4}, implying high purity of Ag nanoparticles which confirmed the contribution of phenolic compounds and ILs in the reduction Ag⁺ to Ag⁰. Antioxidant in the phenolic compounds and abundance of ions in ILs contribute to the synergistic effect of the reduction process (Irfan et al., 2017; Moteriya and Chanda, 2017). The size of the catalyst was estimated by the Debye–Scherrer formula in Eq. (2) based on this primary peak (1 1 1).

$$D = \frac{k\lambda}{\beta \cos \theta} \tag{2}$$

where D is the mean size of the ordered (crystalline) domains, λ is the wavelength of X-ray radiation, k refers to the Scherrer's

constant with the value of 0.9, θ is the Bragg angle and β is the full width at half maximum intensity in of the (1 1 1) plane in radians. The average particle size obtained is approximately 8 nm, 20 nm, 25 nm and 32 nm for Ag_{BF4}, Ag_{TF2N}, Ag_{EtSO4}, and Ag_B, respectively. As observed, the particle size of the Ag nanoparticles was influenced by the type of ILs used for the synthesis process, which may due to the effect of alkyl chain length in imidazolium and anion type of the ionic liquids (Trindade et al., 2014). Apparently, the uses of ILs during synthesis of nanoparticles give a much smaller size of the particle (10–23 nm) as compared with nanoparticles prepared without ILs (40 nm). This is expected due to the application of IL solvent during the synthesis process that created a protective layer around particle and restrict the growth of nanoparticles which resulted to the small particle size (Tzani et al., 2017). Study by Husanu et al. (2018) also claimed that IL-capped silver nanoparticles create diminutive particles with the average size of 8 nm. This proved that the synergistic effect between the phenolic compound from plant extract and the implementation of IL may effectively synthesized nanoparticles while alter the size accordingly depends on the particular ILs used.

3.2.2. Transmission electron microscopy (TEM)

The morphology of the synthesized Ag nanoparticles was examined by using transmission electron microscopy (TEM) as illustrated in Fig. 2. It can be perceived that all the images presented in Fig. 2 show sphere-like structures of the nanoparticles. The TEM image of the Ag_{TF2N}, Ag_{BF4}, and Ag_{EtSO4} demonstrated that the nanoparticles were dispersed with the size of the particle was determined as 8 nm, 20 nm, and 25 nm, respectively. However, Ag_B nanoparticle shows the agglomerated appearance of nanoparticles with the size of 30 nm. It was clearly observed that the size of nanoparticles was affected by the length of alkyl chain in imidazolium. [BMIM⁺] has a long alkyl chain that consists of 4 carbon atoms (C4) as compared with [EMIM⁺] that consist of 2 carbon atoms (C2). Thus, the long alkyl chain can provide an additional steric protection for the formation of Ag_{TF2N} and Ag_{BF4} nanoparticles which reduced the possibility of the aggregation and led to the small particle size (Mazierski et al., 2017). However, despite having the same length of alkyl chain, the nanoparticle sizes differ
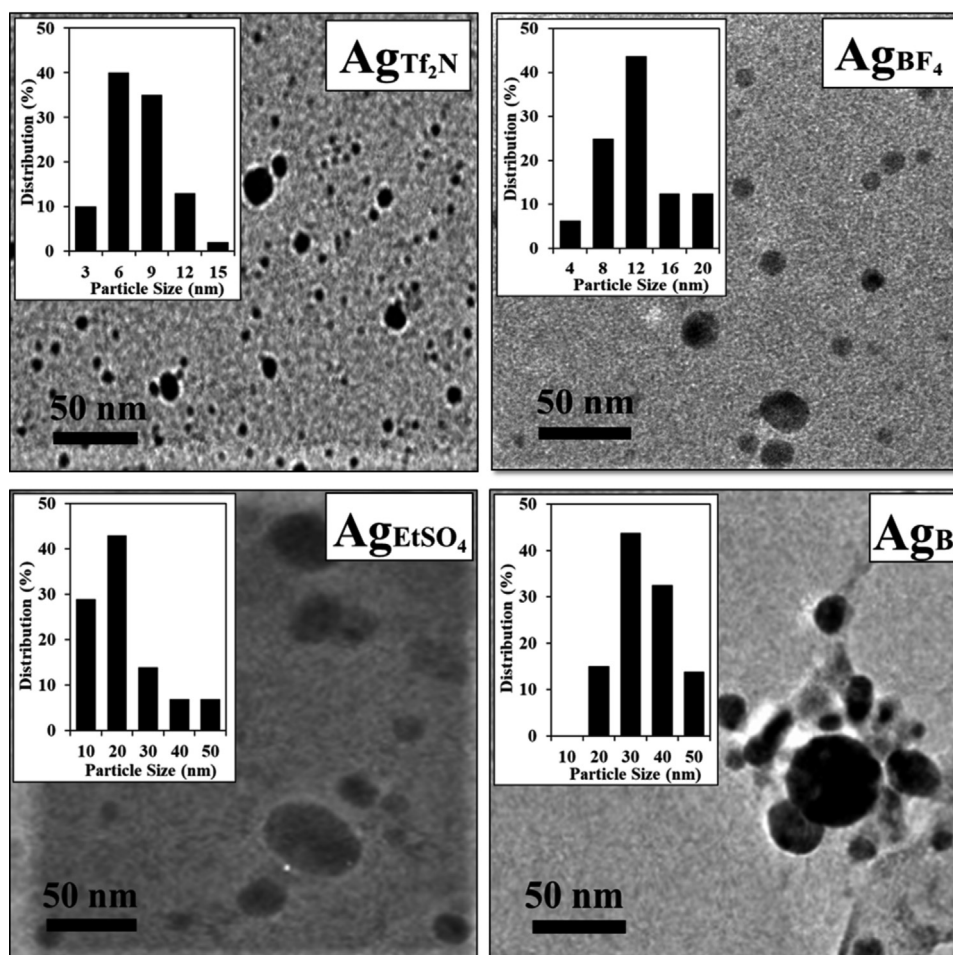
Fig. 2 – TEM images of (A) Ag$_{TF2N}$; (B) Ag$_{BF4}$; (C) Ag$_{EtSO4}$ and (D) Ag$_B$ prepared in OS leaves extract.

Table 1 – Size and surface area of catalysts.

Catalyst	Surface area (m^2/g)	Size (nm)[a]
Ag$_B$	9.34	30
Ag$_{EtSO4}$	7.35	25
Ag$_{BF4}$	11.03	20
Ag$_{TF2N}$	11.92	8

[a] Size of particle was obtained from the TEM analysis.

significantly possibly due to the type of anion of the ILs (Tf$_2$N and BF$_4$). Based on the results, Ag$_{TF2N}$ has the smaller particle size as compared with Ag$_{BF4}$ which is believed due to the large structure of Tf$_2$N that increased the distance between particles and reduce the possibility of agglomeration which subsequently resulted to the small particle size (Goutam et al., 2018). Therefore, it was significantly verified that the presence of ILs can produce much smaller particle size, while the length of alkyl chain, as well as the type of IL anion, gave a consequence to the size and morphology of the Ag nanoparticles.

3.2.3. Surface area analysis

The Brunauer–Emmett–Teller (BET) analysis was carried out in order to determine the surface area of Ag$_{TF2N}$, Ag$_{BF4}$, Ag$_{EtSO4}$ and Ag$_B$ nanoparticles. The results illustrated in Table 1 show that the surface area of nanoparticles was obtained in the following order; Ag$_{TF2N}$ > Ag$_{BF4}$ > Ag$_{EtSO4}$ > Ag$_B$, which suggested that small particle size led to the large surface area. These results were in agreement with the TEM analysis which shows that Ag$_{TF2N}$ has the smallest particle size, followed by Ag$_{BF4}$,

Ag$_{EtSO4}$, and Ag$_B$ nanoparticles. Large surface area of nanoparticles was believed to contain a number of active site on the surface (Boukhatem et al., 2017), which may enhance the adsorption capacity towards organic pollutants.

3.2.4. Fourier transform infrared (FTIR)

The chemical components in the prepared Ag nanoparticles were identified by Fourier transform infrared (FTIR) spectroscopy. Fig. 3 demonstrates the FTIR spectra of the synthesized Ag nanoparticles. The peak at 3348 cm^{-1} was corresponding to the O—H stretching of the polyphenol present in OS leaves extract (Tshemese et al., 2018). The peak located at 1332 cm^{-1} and 1045 cm^{-1} were attributed to the —C—O stretching of —COOH and —C—O—C group, which confirmed the contribution of phenolic compounds in the reduction of silver ions (Ag$^+$) to metallic silver (Ag^0) using (Hoskote Anand and Mandal, 2015). Another peak was noticed at 1127 cm^{-1} which assigned to stretching vibration of C—N from imidazolium ring of ILs (Patil and Murthy, 2016). The appearance of the new peak at 502 cm^{-1} may attributed to the stretching vibrations of Ag—O which remarkably indicated the formation of Ag nanoparticles that either bonded to phenolic compounds of plant extract or the ILs anion (Hu et al., 2014; Niu et al., 2016). This result of binary solvents verified the synergistic effect of the plant extract that promotes the reduction process of Ag$^+$ to Ag^0, while the presence of ILs provides more excellent tenacity against agglomeration which resulted to the discrete and diminutive nanoparticles (Goutam et al., 2018).
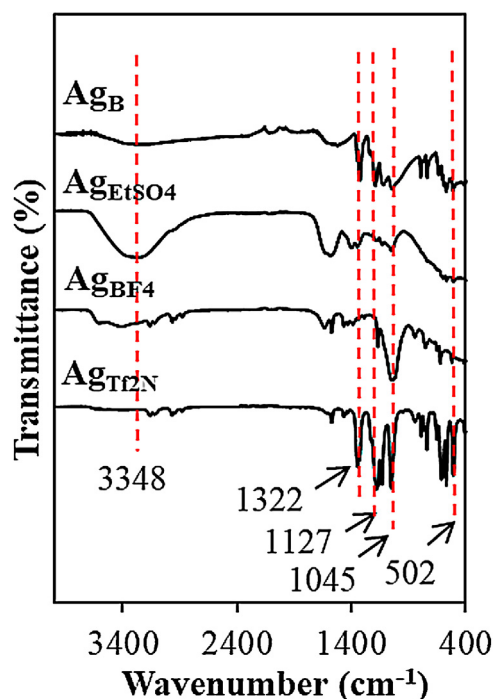
Fig. 3 – (A) FTIR spectra of Ag nanoparticle.

3.3.   *Adsorption and photocatalytic performance*

The performance of the prepared Ag$_{TF2N}$, Ag$_{BF4}$, Ag$_{EtSO4}$ and Ag$_B$ nanoparticles was evaluated on 2,4-D degradation as illustrated in Fig. 4A and B. All catalysts were stirred constantly for 30 min in the dark to achieve adsorption–desorption equilibrium before being exposed to UV-light radiation for 3 h. It can be observed that all catalysts have better performance under UV-light irradiation as compared to being in darkness. The results show that the percentage removal for 2,4-D by Ag$_{TF2N}$, Ag$_{BF4}$, Ag$_{EtSO4}$ and Ag$_B$ after adsorption for 30 min under dark (adsorption–desorption equilibrium) are calculated to be 10.2%, 2.75% 2.94%, and 0.96%, respectively. The

low percentage removal of 2,4-D perceived that the adsorption does not play an important role in the removal of 2,4-D from the aqueous solution. After adsorption–desorption equilibrium, the overall removal of 2,4-D by Ag$_{TF2N}$, Ag$_{BF4}$, Ag$_{EtSO4}$ and Ag$_B$ under light irradiation for 180 min further increased to 65.61%, 52.78%, 49.13% and 37.78%. 82.8%, respectively, indicating the importance of UV-light to the reaction. In addition, the obtained results indicated that the introduction of ILs during synthesis of nanoparticles resulted in the small particle size and subsequently enhance the photocatalytic activity. As mentioned, this happened due to the combination of both ILs and phenolic compounds play an indispensable role as a capping agent and control the size formation of the particle. However, it was also perceived that the alkyl chain length in the imidazolium cation and the type of IL anion used to contribute to the photocatalytic activity of the Ag nanoparticles. The results obviously show that Ag$_{TF2}$ nanoparticles have the highest photocatalytic activity due to the long alkyl chain of the [BMIM$^+$] and large structure of [Tf$_2$N$^-$]; meanwhile, [EMIM$^+$] which has the shortest alkyl chain has a low photocatalytic activity of Ag$_{EtSO4}$ nanoparticles. ILs with the longer alkyl chain and large structure of anion can provide better separation between particles and reduced the possibility of aggregation as compared with ILs that has shorter alkyl chain and small structure of anion which resulted to the less protection towards nanoparticles due to the lack of stabilization in aqueous medium (Trindade et al., 2014). Thus, there is no sufficient repulsion between the Ag particles which lead to the aggregates formation. Consequently, it is resulted in the increase of particle size and reduces the photocatalytic activity. These results also in agreement with the TEM analysis which displays that long alkyl chain length of imidazolium with the larger structure of anion has the smaller sizes of the particle. A recent review of the literature on this topic also reported the effect of the length of the cationic alkyl chain on the degradation rates (Bedia et al., 2019). They stated that the longer the alkyl chains the higher degradation rate ([Dcmim] > [Bmim] > [Emim]). Therefore, it was convinced that
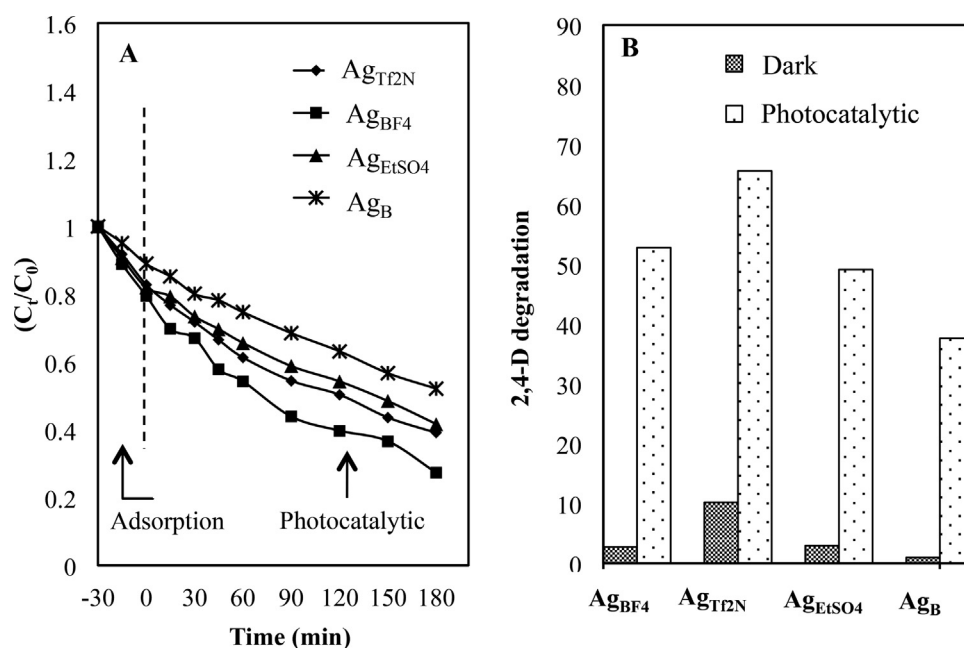

Fig. 4 – (A) Photocatalytic performance of Ag$_{TF2N}$, Ag$_{BF4}$, Ag$_{EtSO4}$ and Ag$_B$; (B) photocatalytic performance of the catalysts under dark and UV-light irradiation.

Table 2 – Input data for CCD.				
Experiment	pH	Catalyst dosage (g/L)	Concentration 2,4-D ($mg L^{-1}$)	2,4-D degradation (%)
1	2.00	0.005	5.00	66.20
2	2.00	0.005	5.00	67.20
3	4.00	0.005	5.00	81.35
4	4.00	0.005	5.00	81.35
5	2.00	0.015	5.00	55.07
6	2.00	0.015	5.00	55.47
7	4.00	0.015	5.00	74.52
8	4.00	0.015	5.00	72.52
9	2.00	0.005	15.00	58.20
10	2.00	0.005	15.00	58.70
11	4.00	0.005	15.00	68.72
12	4.00	0.005	15.00	67.72
13	2.00	0.015	15.00	34.20
14	2.00	0.015	15.00	34.88
15	4.00	0.015	15.00	53.60
16	4.00	0.015	15.00	53.40
17	2.00	0.010	10.00	72.58
18	4.00	0.010	10.00	84.24
19	3.00	0.005	10.00	89.50
20	3.00	0.015	10.00	78.17
21	3.00	0.010	5.00	90.98
22	3.00	0.010	15.00	79.74
23	3.00	0.010	10.00	96.23
24	3.00	0.010	10.00	96.40
25	3.00	0.010	10.00	91.20
26	3.00	0.010	10.00	96.54

the synergistic effect of both ILs and phenolic compounds and the effect of the IL structure can greatly enhance the degradation of 2,4-D. Since the Ag_{TF2N} nanoparticles have the highest photocatalytic activity towards degradation of 2,4-D, this catalyst was used in the subsequent studies of RSM.

3.4. Optimization of the reaction condition using RSM

3.4.1. Statistical analysis and analysis of variance (ANOVA) via CCD

The photodegradation of 2,4-D was optimized using the best catalyst (Ag_{Tf2N}) by response surface methodology (RSM). This design was employed to analyze the influence of three independent factors which are pH, catalyst dosage and initial concentration on the photodegradation of 2,4-D. The specific experimental design and results are shown in Table 2. The regression equation for the photodegradation of 2,4-D is presented in Eq. (3):

$$
\begin{aligned}
\% \, 2,4\text{-D} \ = \ & 94.31 \\
& +7.50A - 7.06B - 7.53C+ \\
& +1.60AB - 0.52AC - 2.42BC \\
& -15.11A^2 - 9.69B^2 - 8.16C^2
\end{aligned}
\tag{3}
$$

The ANOVA analysis was performed in order to assess the statistical significance of the CCD model. The summary of ANOVA results (Table S2) demonstrated that the model F-values (F model = 241.30) obtained was larger than the tabulated F-value (F table = 2.5102), implying that the model was statistically significant and most of the variations in the response can be explained by the regression equation (Gururaj Bhadri, 2014; Karambeigi et al., 2015). Besides of the main effect of pH (A), catalyst dosage (B) and concentration 2,4-D (C), the interaction of pH and catalyst dosage (AB), interaction of catalyst dosage and concentration 2,4-D (BC), second

order effect of pH (A^2), second order effect of catalyst dosage (B^2) and second order effect of concentration 2,4-D (C^2) was also insignificant model terms. However, in the case of interaction between pH and 2,4-D concentration (AC), the model term is considered not significant as the p-values are greater than 0.05. Hence, the current model could be considered to be a good model as most of the model terms are significant (Shahmoradi et al., 2018).

The R^2 value of the model was calculated as 0.9927, this means that the model was explained 99% of the variability in the data (Jusoh et al., 2015b). The values of predicted R^2 (0.9818) were also relatively similar with the values of adjusted R^2 (0.9886) which signifying that this model was a good statistical one (Burin et al., 2013; Fratoddi et al., 2018). Meanwhile, the ratios obtained for adequate precision were 50.17 which are greater than 4, indicating adequate model discrimination and this model can be used to navigate the design space. The results from the actual against predicted plot shown in Fig. 5A also displayed an excellent correlation between actual values with the predicted values due to the most of the points were located on the straight line of the plot. Therefore, the models are considered adequate for the predictions and optimization of the process (Demirel and Kayan, 2012). Furthermore, the plot of the normal probability of the residual for 2,4-D was also illustrated in Fig. 5B in order to analyze the competence fit for the proposed model. The trend shown in this figure reveals the normal distribution of residuals with acceptable equal variance.

3.4.2. Effect of variables as response surface and contour plots

The perturbation plot presented in Fig. 5C was used to study the effect of independent variables which are including pH (A), catalyst dosage (B) and 2,4-D concentration (C) towards photodegradation of 2,4-D. The most significant variables on
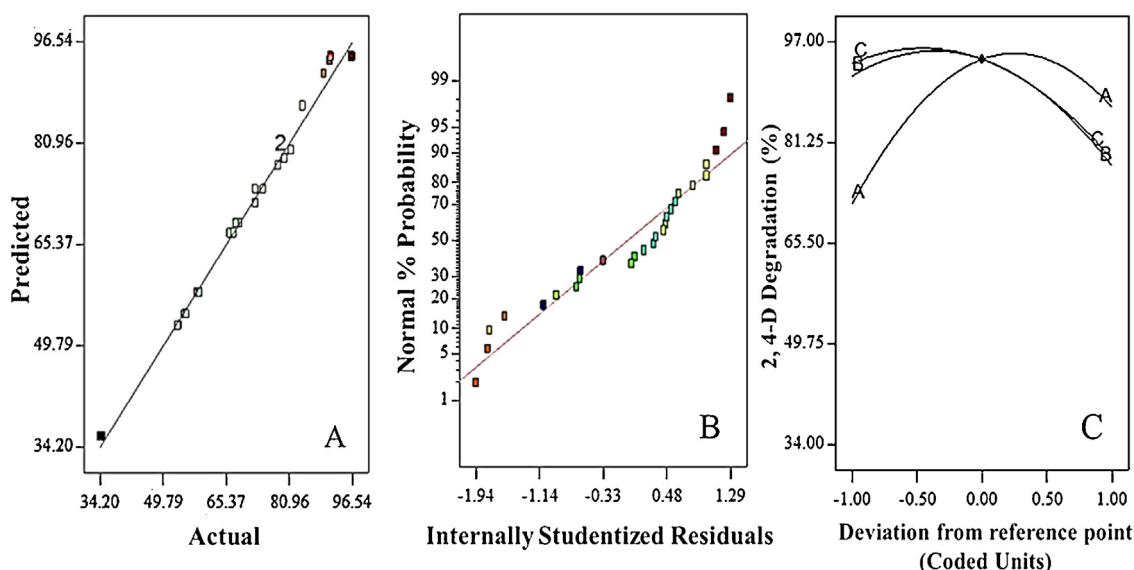
Fig. 5 – (A) The actual and predicted values; (B) normal probability plots; (C) perturbation plot of 2,4-D photodegradation using Ag$_{Tf2N}$ nanoparticles.

the response can be observed through the perturbation plot with a steep slope or curvature indicating that this variable has a remarkable effect on the response (Jawad et al., 2014). Meanwhile, the relatively straight line variable showing that no significant effect in that particular variable (Shahmoradi et al., 2018). From the figure, it can be seen that all the variables (pH, catalyst dosage and concentration of 2,4-D) have steep curvatures revealing the fact that these variables give remarkably consequence on the removal of 2,4-D.

The contour and three-dimensional surface plots were plotted in order to examine the interaction between all three variables. The results obtained for the entire 3D plot shown a good interaction between each independent variable as the response surface plot was found to be elliptical (Savasari et al., 2015). Fig. 6A and B reveals that maximum 2,4-D degradation (>95%) was achieved at pH and catalyst dosage around 3.33 and 0.0075 g/L, respectively. In general, this result could be explained due to the availability of more surface area and specific adsorption sites when catalyst dosage was increased (Lin et al., 2018). However, degradation efficiency of 2,4-D started to declined when catalyst dosage beyond 0.0075 g/L, this is due to the turbidity of the solution that can reduce light penetration and inhibits degradation of 2,4-D (Mahmoodi, 2013, 2014). The previous study also reported that the degradation efficiency of 2,4-D escalated with increasing catalyst dosage up to a certain level (Sharma and Basu, 2020). Meanwhile, the 2,4-D degradation efficiency was found maximum at low pH around 3.33 and further increase the value of pH will reduce the degradation efficiency of 2,4-D. At low pH values, Ag catalyst surface was set to be a positive charge (cation) as the point of zero charges (pH$_{zpc}$) of Ag catalyst has previously determined to be at pH 6.3 (Jaafar et al., 2015). This condition favors the adsorption of 2,4-D anion on to the surface of the Ag catalyst and subsequently increases the degradation efficiency of 2,4-D. This finding is in line with other studies by Ahmed et al. (2020) which depicted that the maximum Alizarin yellow R dye removal by Fe nanoparticles was obtained at low pH rather than high pH.

The effect of pH and 2,4-D concentration (mg L^{-1}) on 2,4-D degradation efficiency is depicted in Fig. 6C and D. From this

result, it was found that more than 95% of 2,4-D degradation were obtained at pH and 2,4-D concentration around 3.33 and 7.50 mg L^{-1}, respectively. The similar effect was noticed in the case of pH which the 2,4-D degradation efficiency started to decline at high pH value. In addition, the obtained results also exhibited the degradation of 2,4-D was significantly influenced by initial 2,4-D concentration. The 2,4-D degradation efficiency elevated when the 2,4-D concentration increases up to around 7.50 mg L^{-1} but further increase of 2,4-D concentration led to decreasing in 2,4-D degradation efficiency. This might be due to the saturation of the surface active site with the adsorbate molecule caused shielding of light radiation (Savasari et al., 2015). Hence, slower production of hydroxyl radical (HO•) that are required to oxidize 2,4-D molecules which resulting in decreasing of 2,4-D degradation efficiency (Shirzad-Siboni et al., 2017). Previously, Nasseh et al. (2020) has studied the effect of tetracycline (TC) concentration in the photocatalytic process. The trends of the results obtained were also similar with the current study, which the efficiency of degradation declined with the increases of TC concentration. The 3D plot showing the effect of catalyst dosage and 2,4-D concentration on the degradation of 2,4-D was demonstrated in Fig. 6E and F. An increase in the catalyst dosage and initial concentration resulted in the intensifying in 2,4-D degradation. However, the 2,4-D degradation started to decline after reached the maximum point of catalyst dosage and 2,4-D concentration around 0.008 g/L and 8.2 mg L^{-1} respectively. This behavior might be related to the ability of the Ag catalyst to absorb 2,4-D molecule with the increasing of the surface active site.

The process optimization modelling suggested that optimum percentage removal of 2,4-D is 97.80% at pH 3.24, catalyst dosage of 0.009 g/L and 2,4-D concentration of 8.15 mg L^{-1} (Table S3). The validation of the developed model was verified by performing additional experiments according to the optimum conditions of the 2,4-D degradation (Table S4). Hence, the corresponding experimental value of 2,4-D degradation under the optimum condition was determined as 96.54% with the percentage error of 1.28%. This study was compared with other previous findings on the optimization of photodegradation
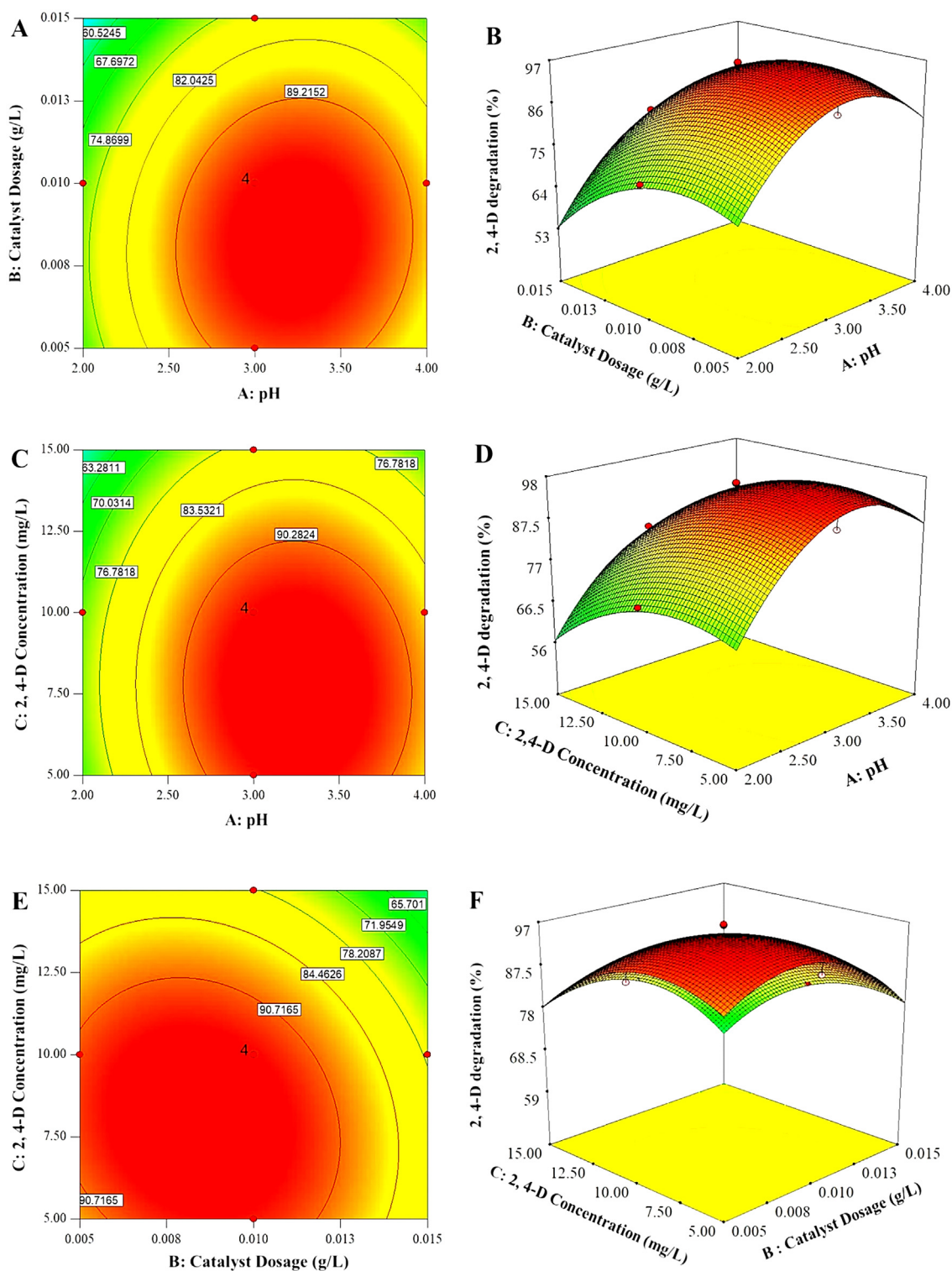
Fig. 6 – Contour and response surface plots for the effect of different variables on 2,4-D degradation.

using central composite design (CCD) with various photocatalyst as listed in Table 3.

3.5. Photocatalytic kinetic studies

3.5.1. Zero order
The kinetic of 2,4-D degradation using Ag nanoparticles was first investigated using zero order kinetic reaction (Talebi et al., 2017). The general rate law expressions are given in Eq. (4):

$$-\frac{d(2,4\text{-D})}{dt} = k_r(2,4\text{-D})^n \tag{4}$$

The differential form of the rate law with $n = 0$ was written as shown in Eq. (5):

$$-\frac{d(2,4-\text{D})}{dt} = k \tag{5}$$

Then, Eq. (5) was integrated and rearranged to Eq. (6):

$$(2,4\text{-D})_0 - (2,4\text{-D})_t = k_0 t \tag{6}$$

The graphs of different 2,4-D concentration at 5, 7.5, 10, 12.5 and 15 ppm were plotted according to zero order kinetic (Eq.
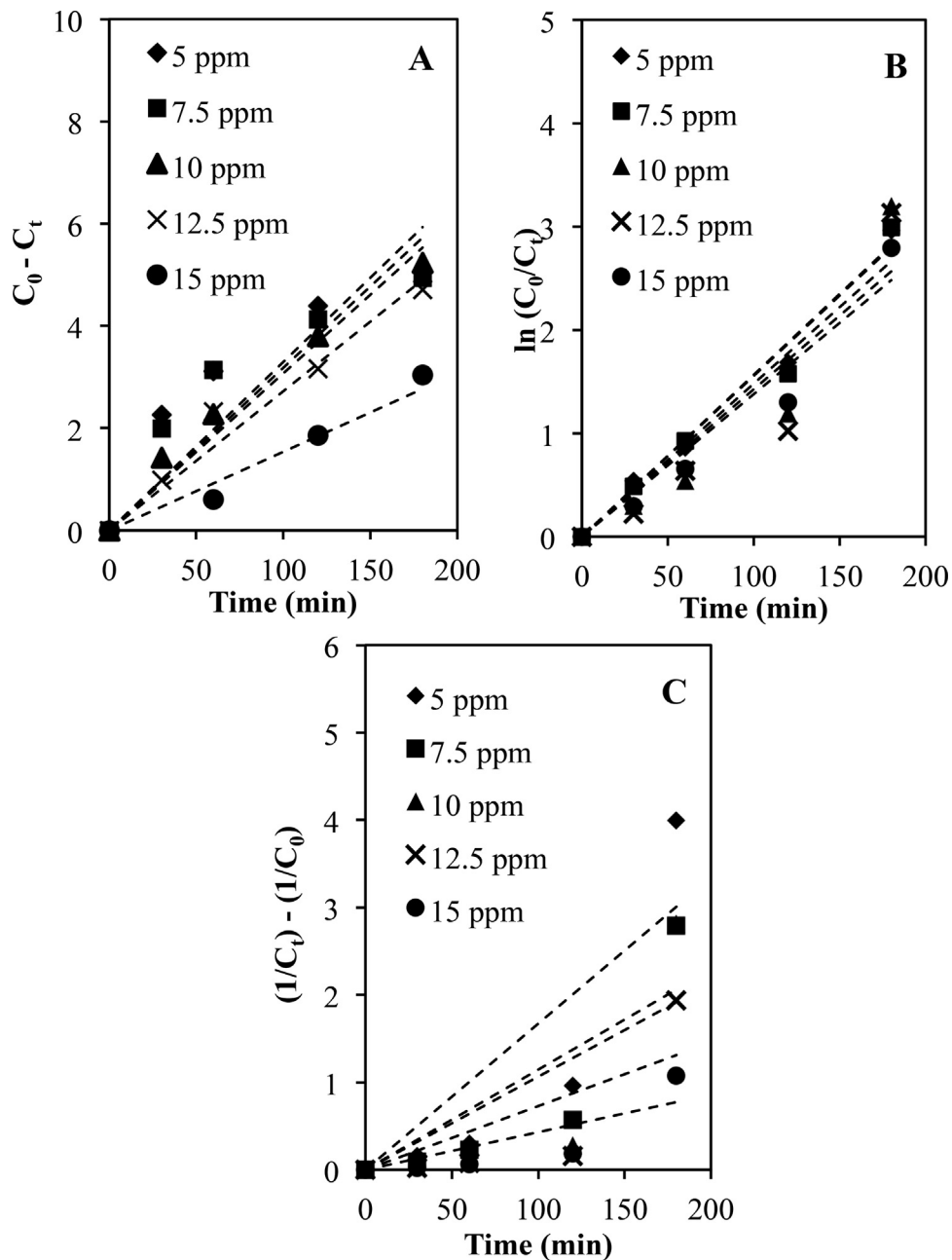
Fig. 7 – The plot of (A) zero order; (B) pseudo-first order and (C) second order kinetic models.

(6)) as demonstrated in Fig. 7A. Meanwhile, the zero order (k_0) rate constants as well as the correlation coefficient (R^2) were studied and tabulated in Table 4.

3.5.2. Eley-Rideal (E–R)

In addition to the zero order kinetic models, the kinetics of the photocatalytic degradation process was also investigated by Eley–Rideal (E–R) kinetic model. Eley–Ridel is one of the most common kinetic model that was used to explain the kinetics of photocatalytic degradation process in aqueous solution (Jorfi et al., 2016; Mosleh et al., 2018). According to the Eley–Rideal (E–R) mechanism, there are two steps involved in the surface-catalyzed reaction which the first step involving the absorption of the gaseous reactant (oxygen) at the surface of catalyst (Saeed et al., 2018). Meanwhile, the second step was related to the reaction that takes place through the creation of positive hole (h⁺) in valence band and photo excited electron (e⁻) in the conduction band of catalyst by irradiation. After that, the photo excited electron was reacted with adsorbed

oxygen and produces superoxide anions (O_2^-). This superoxide anion was then transform to OH• radical through a series of reaction (Saeed et al., 2019a,b). Similarly, the positive hole was reacting with water or hydroxide which led to the formation of OH• radical. These OH• radicals play a significant performance in the degradation of 2,4-D. The rate expression for the Eley–Rideal mechanism can be written as shown in Eq. (7):

$$-\frac{d(2,4\text{-D})}{dt} = k_r O_{2(ad)}(2,4\text{-D})^n \tag{7}$$

By assuming O_2 is constant, Eq. (7) was simplified to Eq. (8)

$$-\frac{d(2,4\text{-D})}{dt} = k(2,4\text{-D})^n \tag{8}$$

After considering the reaction is the 1st order ($n = 1$) and 2nd order ($n = 2$), Eq. (8) was integrated and simplified to a pseudo-

Table 3 – Comparison of the central composite design (CCD) studies with other literature data using various photocatalyst.

Catalyst	Synthesis method	Catalyst size (nm)	Target pollutant	pH	Catalyst dosage (g/L)	Initial concentration (mg L^{-1})	Efficiency (%)	Source
IL-Ag$_{OS}$	Electrolysis	8–25	2,4-Dichlorophenoxyacetic acid	3.24	0.009	8.15	97.8	This study
GO/Fe$_3$O$_4$/TiO$_2$-NiO	Sol–gel	20–35	Imidacloprid	9	0.08	5	97.47	Soltani-nezhad et al. (2019)
TiO$_2$–Fe$_2$O$_3$	Impregnation assisted ultrasonic	15–30	Tetracycline	N/A	0.61	13.86	79.75	Galedari et al. (2019)
N–TiO$_2$	Hydrothermal	12–20	Norfloxacin	6.37	0.54	6.03	99.53	Jin et al. (2019)
BFO/Mr-cl-poly(AAm)-IPN-poly(AA)	Template-induced citrate-based sol–gel process.	58	Coomassie brilliant blue G-250 dye	7	40	10	88.6	Kaith et al. (2018)
IL-Fe$_2$O$_3$/TiO$_2$	Sol–gel method	N/A	Bisphenol A	9	0.75	10	90.33	Asadi et al. (2020)
ZnO@g-C$_3$N$_4$	Solvothermal	N/A	Sulfamethoxazole	5.6	0.65	N/A	90.4	Mirzaei et al. (2018)
Sm-CdS	Ultrasound-assisted co-precipitation	45.7	Acid Red 1	4	1	15	83	Khosroshahi and Mehrizad (2019)

Table 4 – Values of the squared correlation coefficient and rate constant for photocatalytic degradation of 2,4-D.

Initial concentration of 2,4-D (ppm)	Zero order kinetic ($C_0 - C = kt$)		Eley–Rideal (E–R)				
			Pseudo-first order kinetic ($\ln(C/C_0) = kt$)		Second order kinetic ($1/C - 1/C_0 = kt$)		
	k_0 (mg min^{-1} L^{-1})	R_0^2	k_1 (min^{-1})	R_1^2	k_2 (L mg^{-1} min^{-1})	R_2^2	
5	0.0330	0.7527	0.0157	0.9870	0.0167	0.7589	
7.5	0.0318	0.7769	0.0156	0.9776	0.0115	0.7331	
10	0.0307	0.9676	0.0148	0.8830	0.0106	0.6305	
12.5	0.0272	0.9592	0.0143	0.8602	0.0073	0.6202	
15	0.0154	0.8575	0.0138	0.9464	0.0043	0.7030	

first order equation (Eq. (9)) and second order equation (Eq. (10)) as reported by other studies (Begum et al., 2018, 2016).

$$\ln \frac{(2,4\text{-}D)_0}{(2,4\text{-}D)_t} = k_1 t \qquad (9)$$

$$\frac{1}{(2,4\text{-}D)_t} - \frac{1}{(2,4\text{-}D)_0} = k_2 t \qquad (10)$$

The graphs of pseudo-first order and second order kinetic were plotted as demonstrated in Fig. 7B and C. The pseudo-first order rate constant (k_1) and second order rate constant (k_2) were obtained from the slope of the plot. Table 4 indicates that a high correlation coefficient, R^2 was achieved when degradation of 2,4-D was studied using pseudo-first order kinetic model ($R^2 > 0.98$). Meanwhile, the lower R^2 values for zero-order ($R^2 > 0.96$) and second-order kinetic ($R^2 > 0.75$) confirming a poor applicability of the kinetic model to represent the kinetics of the photocatalytic degradation of 2,4-D. The obtained results also show that the rate of degradation decreases with increase in concentration of 2,4-D. The decrease in rate constant is due to the amount of generated radical on the surface of catalyst reduced as high concentration of 2,4-D molecules caused shielding of light radiation (El Hassani et al., 2019). In addition, the increases of 2,4-D concentration would produce high amount of intermediates, leading to the upsurge in consumption of OH$^\bullet$ radicals and consequently initiate a retardation effect on degradation efficiency (Saeed et al., 2020). Therefore, based on the comparison of the correlation coefficient, R^2 between these three kinetic reaction, the pseudo-first order kinetic illustrated the best fitting model to the process of 2,4-D degradation ($R^2 > 0.98$) which positively predicted the constant elimination amount of 2,4-D throughout the photocatalytic process.

4. Conclusion

The Ag nanoparticle namely Ag_{Tf2N}, Ag_{BF4} and Ag_{EtSO4} synthesized using binary solvents of OS leaves extract with different ILs of [BMIM Tf$_2$N], [BMIM BF$_4$] and [EMIM EtSO$_4$], respectively, were found to be smaller and effective for catalytic reduction of 2,4-D. The characterization analysis of the nanoparticles was compared with Ag_B via XRD, TEM, BET, and FTIR. The XRD analysis confirmed high crystallinity of the synthesized Ag nanoparticles, suggesting the contribution of phenolic compounds and ILs in the reduction of silver ions (Ag$^+$) to metallic silver (Ag^0), aside having the ability to alter the size of the nanoparticles. [BMIM Tf$_2$N] positively produced smaller size of Ag_{Tf2N} (8 nm), compared to the one synthesized using [BMIM BF$_4$] and [EMIM EtSO$_4$], obtaining larger sizes of nanoparticles at 20 nm (Ag_{BF4}) and 25 nm (Ag_{EtSO4}), respectively. Significantly, the FTIR verified the formation of Ag—O bonds at peak 502 cm^{-1}. Meanwhile, the TEM images implying that long alkyl chain of imidazolium anion and large structure of anion can prevent the aggregation of nanoparticles which resulted in the distinct and diminutive of Ag particles. In term of photocatalytic activity, Ag_{Tf2N} nanoparticles gave the highest photocatalytic activity (65.61%), followed by Ag_{BF4} (52.78%), Ag_{EtSO4} (49.13%) and Ag_B (37.78%). Based on the observation, it was convinced that the photocatalytic activity of the Ag nanoparticles was greatly affected by the presence of ILs as well as the alkyl chain length and the type of IL anion. Long alkyl chain with a large structure of anion produced the small size of Ag particle which led to the enhancement

of the photocatalytic activity. Optimization by response surface methodology shows that the highest degradation of 2,4-D (97.80%) was obtained at pH 3.24, catalyst dosage of 0.009 g/L and 2,4-D concentration of 8.15 mg L^{-1} with validation experiments of 1.28% error. The kinetic studies suggested that 2,4-D degradation was fitted well with the pseudo-first order kinetic reaction with the values of $R^2 > 0.98$ which positively predicted the constant elimination amount of 2,4-D throughout the photocatalytic process.

The current study indicated that the uses of binary solvent; ILs and plant extract played an important role in synthesized of well-dispersed and diminutive Ag nanoparticles which subsequently enhancing the photocatalytic reaction. However, the stability and recoverability of the catalyst need to further studied as sometimes the diminutive of nanoparticles may induce to the agglomeration and affect the photocatalytic activity. In addition, in this study the Ag nanoparticles were not supported with semiconductor nanoparticles or any supported-materials and it found that Ag can be unstable under chemical reactions due the sintering of particles. Therefore, highly ordered and uniform metallic nanoparticles on support substrates are highly demanded as better control in the uniformity and distribution of the nanoparticles leads to better controlled properties. Further investigation in this area may contribute to understanding the potential of ILs and plant extract as an effective media to obtain an excellent Ag catalyst for the abatement of organic pollutants through photocatalytic degradation.

Conflict of interests

The authors declare that they have no known competing financial interests or personal relationships that could have appeared to influence the work reported in this paper.

Acknowledgements

Appendix A. Supplementary data

Supplementary material related to this article can be found, in the online version, at https://doi.org/10.1016/j.cherd.2020.03.025.

References

Ahmed, A., Usman, M., Yu, B., Ding, X., Peng, Q., Shen, Y., Cong, H., 2020. Efficient photocatalytic degradation of toxic Alizarin yellow R dye from industrial wastewater using biosynthesized Fe nanoparticle and study of factors affecting the degradation rate. J. Photochem. Photobiol. B: Biol. 202, 111682.

Ali, T., Ahmed, A., Alam, U., Uddin, I., Tripathi, P., Muneer, M., 2018. Enhanced photocatalytic and antibacterial activities of Ag-doped TiO$_2$ nanoparticles under visible light. Mater. Chem. Phys. 212, 325–335, http://dx.doi.org/10.1016/j.matchemphys.2018.03.052.

Ambika, S., Sundrarajan, M., 2016. [EMIM] BF4 ionic liquid-mediated synthesis of TiO$_2$ nanoparticles using Vitex negundo Linn extract and its antibacterial activity. J. Mol. Liq. 221, 986–992, http://dx.doi.org/10.1016/j.molliq.2016.06.079.

Ariff, M.A.M., Alrozi, R., Saleh, M.H., Razak, N.A., Osman, M.S., Zamanhuri, N.A., 2012. Green biosynthesis of nanosilvers using aqueous extract from *Orthosiphon stamineus* leaves. SHUSER 2012 – 2012 IEEE Symposium on Humanities, Science and Engineering Research, 1115–1119, http://dx.doi.org/10.1109/SHUSER.2012.6268790.

Asadi, A.M.S., Malakootian, M., Kowsari, E., Alidadi, H., 2020. Ionic liquid-assisted sol–gel synthesis of Fe_2O_3–TiO_2 for enhanced photocatalytic degradation of bisphenol A under UV illumination: modeling and optimization using response surface methodology. Optik, 164229.

Bedia, J., Rodriguez, J.J., Moreno, D., Palomar, J., Belver, C., 2019. Photostability and photocatalytic degradation of ionic liquids in water under solar light. RSC Adv. 9 (4), 2026–2033.

Begum, R., Najeeb, J., Ahmad, G., Wu, W., Irfan, A., Al-Sehemi, A.G., Farooqi, Z.H., 2018. Synthesis and characterization of poly (N-isopropylmethacrylamide-co-acrylic acid) microgels for in situ fabrication and stabilization of silver nanoparticles for catalytic reduction of o-nitroaniline in aqueous medium. React. Funct. Polym. 132, 89–97.

Begum, R., Naseem, K., Ahmed, E., Sharif, A., Farooqi, Z.H., 2016. Simultaneous catalytic reduction of nitroarenes using silver nanoparticles fabricated in poly (N-isopropylacrylamide-acrylic acid-acrylamide) microgels. Colloids Surf. A: Physicochem. Eng. Asp. 511, 17–26.

Bezares, I., Del Campo, A., Herrasti, P., Muñoz-Bonilla, A., 2015. A simple aqueous electrochemical method to synthesize TiO_2 nanoparticles. Phys. Chem. Chem. Phys. 17 (43), 29319–29326, http://dx.doi.org/10.1039/c5cp05525c.

Boukhatem, H., Khalaf, H., Djouadi, L., Gonzalez, F.V., Navarro, R.M., Santaballa, J.A., Canle, M., 2017. Photocatalytic activity of mont–La (6%)–Cu0.6Cd0.4S catalyst for phenol degradation under near UV visible light irradiation. Appl. Catal. B: Environ. 211, 114–125, http://dx.doi.org/10.1016/j.apcatb.2017.03.074.

Burin, V.M., Marchand, S., De Revel, G., Bordignon-Luiz, M.T., 2013. Development and validation of method for heterocyclic compounds in wine: optimization of HS-SPME conditions applying a response surface methodology. Talanta 117, 87–93, http://dx.doi.org/10.1016/j.talanta.2013.08.037.

Corrêa, C.M., Bizeto, M.A., Camilo, F.F., 2016. Direct synthesis of silver nanoparticles in ionic liquid. J. Nanopart. Res. 18 (5), 132.

Dehghani, M.H., Faraji, M., Mohammadi, A., Kamani, H., 2017. Optimization of fluoride adsorption onto natural and modified pumice using response surface methodology: isotherm, kinetic and thermodynamic studies. Korean J. Chem. Eng. 34 (2), 454–462, http://dx.doi.org/10.1007/s11814-016-0274-4.

Demirel, M., Kayan, B., 2012. Application of response surface methodology and central composite design for the optimization of textile dye degradation by wet air oxidation. Int. J. Ind. Chem. 3 (1), 1–10, http://dx.doi.org/10.1186/2228-5547-3-24.

Denrah, S., Sarkar, M., 2019. Design of experiment for optimization of nitrophenol reduction by green synthesized silver nanocatalyst. Chem. Eng. Res. Des., 494–504, http://dx.doi.org/10.1016/j.cherd.2019.02.021.

El Hassani, K., Kalnina, D., Turks, M., Beakou, B.H., Anouar, A., 2019. Enhanced degradation of an azo dye by catalytic ozonation over Ni-containing layered double hydroxide nanocatalyst. Sep. Purif. Technol. 210, 764–774.

Farrokhnia, M., Karimi, S., Momeni, S., Khalililaghab, S., 2017. Colorimetric sensor assay for detection of hydrogen peroxide using green synthesis of silver chloride nanoparticles: experimental and theoretical evidence. Sensors Actuat. B: Chem. 246, 979–987, http://dx.doi.org/10.1016/j.snb.2017.02.066.

Fattahian, Y., Riahi-Madvar, A., Mirzaee, R., Torkzadeh-Mahani, M., Asadikaram, G., Sargazi, G., 2018. Optimization of in vitro refolding conditions of recombinant Lepidium draba peroxidase using design of experiments. Int. J. Biol. Macromol. 118, 1369–1376, http://dx.doi.org/10.1016/j.ijbiomac.2018.06.122.

Fratoddi, I., Rapa, M., Testa, G., Venditti, I., Scaramuzzo, F.A., Vinci, G., 2018. Response surface methodology for the optimization of phenolic compounds extraction from extra virgin olive oil with functionalized gold nanoparticles. Microchem. J. 138, 430–437, http://dx.doi.org/10.1016/j.microc.2018.01.043.

Galedari, M., Ghazi, M.M., Mirmasoomi, S.R., 2019. Photocatalytic process for the tetracycline removal under visible light: presenting a degradation model and optimization using response surface methodology (RSM). Chem. Eng. Res. Des. 145, 323–333.

González, E.J., Díaz, I., Gonzalez-Miquel, M., Rodríguez, M., Sueiras, A., 2018. On the behavior of imidazolium versus pyrrolidinium ionic liquids as extractants of phenolic compounds from water: experimental and computational analysis. Sep. Purif. Technol. 201, 214–222, http://dx.doi.org/10.1016/j.seppur.2018.03.006.

Goutam, S.P., Saxena, G., Singh, V., Yadav, A.K., Bharagava, R.N., Thapa, K.B., 2018. Green synthesis of TiO_2 nanoparticles using leaf extract of *Jatropha curcas* L. for photocatalytic degradation of tannery wastewater. Chem. Eng. J. 336, 386–396, http://dx.doi.org/10.1016/j.cej.2017.12.029.

Gururaj Bhadri, S.H., 2014. Statistical optimization of medium components by response surface methodology for enhanced production of bacterial cellulose by *Gluconacetobacter persimmonis*. J. Bioprocess. Biotech. 04 (01), http://dx.doi.org/10.4172/2155-9821.1000142.

Hamedi, S., Shojaosadati, S.A., Mohammadi, A., 2017. Evaluation of the catalytic, antibacterial and anti-biofilm activities of the *Convolvulus arvensis* extract functionalized silver nanoparticles. J. Photochem. Photobiol. B: Biol. 167, 36–44, http://dx.doi.org/10.1016/j.jphotobiol.2016.12.025.

Hareesh, K., Joshi, R.P., Dahiwale, S.S., Bhoraskar, V.N., Dhole, S.D., 2016. Synthesis of Ag-reduced graphene oxide nanocomposite by gamma radiation assisted method and its photocatalytic activity. Vacuum 124, 40–45, http://dx.doi.org/10.1016/j.vacuum.2015.11.011.

Hekmati, M., Hasanirad, S., Khaledi, A., Esmaeili, D., 2020. Green synthesis of silver nanoparticles using extracts of *Allium rotundum* l, *Falcaria vulgaris* Bernh, and *Ferulago angulate* Boiss, and their antimicrobial effects in vitro. Gene Rep., 100589.

Hoskote Anand, K.K., Mandal, B.K., 2015. Activity study of biogenic spherical silver nanoparticles towards microbes and oxidants. Spectrochim. Acta – Part A: Mol. Biomol. Spectr. 135, 639–645, http://dx.doi.org/10.1016/j.saa.2014.07.013.

Hu, J., Hu, X., Chen, A., Zhao, S., 2014. Directly aqueous synthesis of well-dispersed superparamagnetic Fe_3O_4 nanoparticles using ionic liquid-assisted co-precipitation method. J. Alloys Compd. 603, 1–6, http://dx.doi.org/10.1016/j.jallcom.2014.02.022.

Husanu, E., Chiappe, C., Bernardini, A., Cappello, V., Gemmi, M., 2018. Synthesis of colloidal Ag nanoparticles with citrate based ionic liquids as reducing and capping agents. Colloids Surf. A: Physicochem. Eng. Asp. 538, 506–512.

Irfan, M., Moniruzzaman, M., Ahmad, T., Mandal, P.C., Bhattacharjee, S., Abdullah, B., 2017. Ionic liquid based extraction of flavonoids from *Elaeis guineensis* leaves and their applications for gold nanoparticles synthesis. J. Mol. Liq. 241, 270–278, http://dx.doi.org/10.1016/j.molliq.2017.05.151.

Jaafar, N.F., Jalil, A.A., Triwahyono, S., 2017. Visible-light photoactivity of plasmonic silver supported on mesoporous TiO_2 nanoparticles (Ag-MTN) for enhanced degradation of 2-chlorophenol: limitation of Ag–Ti interaction. Appl. Surf. Sci. 392, 1068–1077, http://dx.doi.org/10.1016/j.apsusc.2016.09.112.

Jaafar, N.F., Jalil, A.A., Triwahyono, S., Efendi, J., Mukti, R.R., Jusoh, R., ..., Suendo, V., 2015. Direct in situ activation of Ag0 nanoparticles in synthesis of Ag/TiO_2 and its photoactivity. Appl. Surf. Sci. 338, 75–84, http://dx.doi.org/10.1016/j.apsusc.2015.02.106.

Jafari, A.J., Kermani, M., Hosseini-Bandegharaei, A., Rastegar, A., Gholami, M., Alahabadi, A., Farzi, G., 2019. Synthesis and characterization of Ag/TiO_2/composite aerogel for enhanced adsorption and photo-catalytic degradation of toluene from the gas phase. Chem. Eng. Res. Des., http://dx.doi.org/10.1016/j.cherd.2019.07.017.

Jawad, A.H., Alkarkhi, A.F.M., Mubarak, N.S.A., 2014. Photocatalytic decolorization of methylene blue by an immobilized TiO_2 film under visible light irradiation: optimization using response surface methodology (RSM). Desalin. Water Treat. 3994 (September), 1–12, http://dx.doi.org/10.1080/19443994.2014.934736.

Jayarambabu, N., Akshaykranth, A., Rao, T.V., Rao, K.V., Kumar, R.R., 2020. Green synthesis of Cu nanoparticles using *Curcuma longa* extract and their application in antimicrobial activity. Mater. Lett. 259, 126813.

Jin, X., Zhou, X., Sun, P., Lin, S., Cao, W., Li, Z., Liu, W., 2019. Photocatalytic degradation of norfloxacin using N-doped TiO2: optimization, mechanism, identification of intermediates and toxicity evaluation. Chemosphere 237, 124433.

Jini, D., Sharmila, S., 2019. Green synthesis of silver nanoparticles from *Allium cepa* and its in vitro antidiabetic activity. Mater. Today: Proc.

Jorfi, S., Barzegar, G., Ahmadi, M., Darvishi Cheshmeh Soltani, R., Alah Jafarzadeh Haghighifard, N., Takdastan, A., . . ., Abtahi, M., 2016. Enhanced coagulation-photocatalytic treatment of Acid red 73 dye and real textile wastewater using UVA/synthesized MgO nanoparticles. J. Environ. Manage. 177, 111–118, http://dx.doi.org/10.1016/j.jenvman.2016.04.005.

Jusoh, N.W.C., Jalil, A.A., Triwahyono, S., Mamat, C.R., 2015a. Tailoring the metal introduction sequence onto mesostructured silica nanoparticles framework: effect on physicochemical properties and photoactivity. Appl. Catal. A: Gen. 492, 169–176, http://dx.doi.org/10.1016/j.apcata.2014.12.046.

Jusoh, R., Jalil, A.A., Triwahyono, S., Idris, A., Noordin, M.Y., 2015b. Photodegradation of 2-chlorophenol over colloidal α-FeOOH supported mesostructured silica nanoparticles: influence of a pore expander and reaction optimization. Sep. Purif. Technol. 149, 55–64, http://dx.doi.org/10.1016/j.seppur.2015.05.017.

Kadi, M.W., Ismail, A.A., Mohamed, R.M., Bahnemann, D.W., 2018. Photodegradation of the herbicide imazapyr over mesoporous In_2O_3–TiO_2 nanocomposites with enhanced photonic efficiency. Sep. Purif. Technol. 205 (April), 66–73, http://dx.doi.org/10.1016/j.seppur.2018.05.013.

Kaith, B.S., Shanker, U., Gupta, B., Bhatia, J.K., 2018. RSM-CCD optimized In-air synthesis of photocatalytic nanocomposite: application in removal-degradation of toxic brilliant blue. React. Funct. Polym. 131, 107–122.

Karambeigi, M.S., Abbassi, R., Roayaei, E., Emadi, M.A., 2015. Emulsion flooding for enhanced oil recovery: interactive optimization of phase behavior, microvisual and core-flood experiments. J. Ind. Eng. Chem. 29, 382–391, http://dx.doi.org/10.1016/j.jiec.2015.04.019.

Khan, Z., Bashir, O., Hussain, J.I., Kumar, S., Ahmad, R., 2012. Effects of ionic surfactants on the morphology of silver nanoparticles using Paan (*Piper betel*) leaf petiole extract. Colloids Surf. B: Biointerfaces 98, 85–90, http://dx.doi.org/10.1016/j.colsurfb.2012.04.033.

Khosroshahi, A.G., Mehrizad, A., 2019. Optimization, kinetics and thermodynamics of photocatalytic degradation of Acid Red 1 by Sm-doped CdS under visible light. J. Mol. Liq. 275, 629–637.

Kumar, P., Govindaraju, M., Senthamilselvi, S., Premkumar, K., 2013. Photocatalytic degradation of methyl orange dye using silver (Ag) nanoparticles synthesized from *Ulva lactuca*. Colloids Surf. B: Biointerfaces 103, 658–661, http://dx.doi.org/10.1016/j.colsurfb.2012.11.022.

Lin, J., Su, B., Sun, M., Chen, B., Chen, Z., 2018. Biosynthesized iron oxide nanoparticles used for optimized removal of cadmium with response surface methodology. Sci. Total Environ. 627, 314–321, http://dx.doi.org/10.1016/j.scitotenv.2018.01.170.

Liu, B., Li, X., Zhao, Q., Ke, J., Tadé, M., Liu, S., 2016. Preparation of $AgInS_2$/TiO_2 composites for enhanced photocatalytic degradation of gaseous o-dichlorobenzene under visible light. Appl. Catal. B: Environ. 185, 1–10, http://dx.doi.org/10.1016/j.apcatb.2015.12.003.

Liu, X., Li, C., Zhang, Y., Yu, J., Yuan, M., Ma, Y., 2017. Simultaneous photodegradation of multi-herbicides by oxidized carbon nitride: performance and practical application. Appl. Catal. B: Environ. 219, 194–199, http://dx.doi.org/10.1016/j.apcatb.2017.07.007.

Lv, Z., Zhong, Q., Ou, M., 2016. Utilizing peroxide as precursor for the synthesis of CeO_2/ZnO composite oxide with enhanced photocatalytic activity. Appl. Surf. Sci. 376, 91–96, http://dx.doi.org/10.1016/j.apsusc.2016.01.280.

Mahmoodi, N.M., 2013. Photodegradation of dyes using multiwalled carbon nanotube and ferrous ion. J. Environ. Eng. 139 (11), 1368–1374, http://dx.doi.org/10.1061/(asce)ee.1943-7870.0000762.

Mahmoodi, N.M., 2014. Binary catalyst system dye degradation using photocatalysis. Fibers Poly. 15 (2), 273–280, http://dx.doi.org/10.1007/s12221-014-0273-1.

Mazierski, P., Łuczak, J., Lisowski, W., Winiarski, M.J., Klimczuk, T., Zaleska-Medynska, A., 2017. The ILs-assisted electrochemical synthesis of TiO 2 nanotubes: the effect of ionic liquids on morphology and photoactivity. Appl. Catal. B: Environ. 214, 100–113, http://dx.doi.org/10.1016/j.apcatb.2017.05.005.

Mirzaei, A., Yerushalmi, L., Chen, Z., Haghighat, F., 2018. Photocatalytic degradation of sulfamethoxazole by hierarchical magnetic ZnO@g-C_3N_4: RSM optimization, kinetic study, reaction pathway and toxicity evaluation. J. Hazard. Mater. 359, 516–526, http://dx.doi.org/10.1016/j.jhazmat.2018.07.077.

Mosleh, S., Rahimi, M.R., Ghaedi, M., Asfaram, A., Jannesar, R., Sadeghfar, F., 2018. A rapid and efficient sonophotocatalytic process for degradation of pollutants: statistical modeling and kinetics study. J. Mol. Liq. 261, 291–302, http://dx.doi.org/10.1016/j.molliq.2018.03.115.

Moteriya, P., Chanda, S., 2017. Synthesis and characterization of silver nanoparticles using *Caesalpinia pulcherrima* flower extract and assessment of their in vitro antimicrobial, antioxidant, cytotoxic, and genotoxic activities. Artif. Cells Nanomed. Biotechnol. 45 (8), 1556–1567, http://dx.doi.org/10.1080/21691401.2016.1261871.

Muthu, K., Priya, S., 2017. Green synthesis, characterization and catalytic activity of silver nanoparticles using *Cassia auriculata* flower extract separated fraction. Spectrochim. Acta – Part A: Mol. Biomol. Spectrosc. 179, 66–72, http://dx.doi.org/10.1016/j.saa.2017.02.024.

Nasseh, N., Panahi, A.H., Esmati, M., Daglioglu, N., Asadi, A., Rajati, H., Khodadoost, F., 2020. Enhanced photocatalytic degradation of tetracycline from aqueous solution by a novel magnetically separable FeN/SiO_2/ZnO nano-composite under simulated sunlight: Efficiency, stability, and kinetic studies. J. Mol. Liq. 301, 112434, http://dx.doi.org/10.1016/j.molliq.2019.112434.

Niu, W.J., Zhu, R.H., Yan-Hua, Zeng, H.B., Cosnier, S., Zhang, X.J., Shan, D., 2016. One-pot synthesis of nitrogen-rich carbon dots decorated graphene oxide as metal-free electrocatalyst for oxygen reduction reaction. Carbon 109, 402–410, http://dx.doi.org/10.1016/j.carbon.2016.08.002.

Passos, H., Freire, M.G., Coutinho, J.A.P., 2014. Ionic liquid solutions as extractive solvents for value-added compounds from biomass. Green Chem., http://dx.doi.org/10.1039/c4gc00236a.

Patil, H.R., Murthy, Z.V.P., 2016. Preparation of vanadium pentoxide nanoparticles by ionic liquid-assisted sonochemical method: effect of ionic liquid stericity on particle characteristics. Chem. Eng. Process.: Process Intensif. 102, 130–140, http://dx.doi.org/10.1016/j.cep.2016.01.016.

Patil, V., Mahajan, S., Kulkarni, M., Patil, K., Rode, C., Coronas, A., Yi, G.-R., 2020. Synthesis of silver nanoparticles colloids in imidazolium halide ionic liquids and their antibacterial activities for gram-positive and gram-negative bacteria. Chemosphere 243, 125302.

Priya, Kaith, B.S., Shanker, U., Gupta, B., Bhatia, J.K., 2018. RSM-CCD optimized In-air synthesis of photocatalytic nanocomposite: application in removal-degradation of toxic brilliant blue. React. Funct. Polym. 131, 107–122, http://dx.doi.org/10.1016/j.reactfunctpolym.2018.07.016.

Ravichandran, V., Vasanthi, S., Shalini, S., Shah, S.A.A., Tripathy, M., Paliwal, N., 2019. Green synthesis, characterization,

antibacterial, antioxidant and photocatalytic activity of *Parkia speciosa* leaves extract mediated silver nanoparticles. Results Phys. 15, 102565.

Saeed, M., Muneer, M., Akram, N., ul Haq, A., Afzal, N., Hamayun, M., 2019a. Synthesis and characterization of silver loaded alumina and evaluation of its photo catalytic activity on photo degradation of methylene blue dye. Chem. Eng. Res. Des. 148, 218–226, http://dx.doi.org/10.1016/j.cherd.2019.06.020.

Saeed, M., Muneer, M., Khosa, M.K.K., Akram, N., Khalid, S., Adeel, M., . . ., Sherazi, S., 2019b. *Azadirachta indica* leaves extract assisted green synthesis of Ag–TiO$_2$ for degradation of Methylene blue and Rhodamine B dyes in aqueous medium. Green Process. Synth. 8 (1), 659–666.

Saeed, M., Siddique, M., Ibrahim, M., Akram, N., Usman, M., Aleem, M.A., Baig, A., 2020. *Calotropis gigantea* leaves assisted biosynthesis of ZnO and Ag@ ZnO catalysts for degradation of rhodamine B dye in aqueous medium. Environ. Prog. Sustain. Energy, e13408.

Saeed, M., Usman, M., ul Haq, A., 2018. Catalytic degradation of organic dyes in aqueous medium. Photochem. Photophys.: Fundamentals to Applications, 197.

Sapawe, N., Rustam, M.A., Mahadzir, M.H.H., Lani, M.K.E.M., Raidin, A., Hanafi, M.F., 2019. A novel approach of in-situ electrobiosynthesis of metal oxide nanoparticles using crude plant extract as main medium for supporting electrolyte. Mater. Today: Proc. 19, 1441–1445.

Savasari, M., Emadi, M., Bahmanyar, M.A., Biparva, P., 2015. Optimization of Cd (II) removal from aqueous solution by ascorbic acid-stabilized zero valent iron nanoparticles using response surface methodology. J. Ind. Eng. Chem. 21, 1403–1409, http://dx.doi.org/10.1016/j.jiec.2014.06.014.

Shahmoradi, B., Yavari, S., Zandsalimi, Y., Shivaraju, H.P., Negahdari, M., Maleki, A., . . ., Lee, S.M., 2018. Optimization of solar degradation efficiency of bio-composting leachate using Nd: ZnO nanoparticles. J. Photochem. Photobiol. A: Chem. 356, 201–211, http://dx.doi.org/10.1016/j.jphotochem.2018.01.002.

Sharma, S., Basu, S., 2020. Highly reusable visible light active hierarchical porous WO$_3$/SiO$_2$ monolith in centimeter length scale for enhanced photocatalytic degradation of toxic pollutants. Sep. Purif. Technol. 231, 115916.

Shirzad-Siboni, M., Jonidi-Jafari, A., Farzadkia, M., Esrafili, A., Gholami, M., 2017. Enhancement of photocatalytic activity of Cu-doped ZnO nanorods for the degradation of an insecticide: kinetics and reaction pathways. J. Environ. Manage. 186, 1–11, http://dx.doi.org/10.1016/j.jenvman.2016.10.049.

Singh, J., Kumar, V., Kim, K.-H., Rawat, M., 2019. Biogenic synthesis of copper oxide nanoparticles using plant extract and its prodigious potential for photocatalytic degradation of dyes. Environ. Res. 177, 108569.

Soltani-nezhad, F., Saljooqi, A., Shamspur, T., Mostafavi, A., 2019. Photocatalytic degradation of imidacloprid using GO/Fe$_3$O$_4$/TiO$_2$-NiO under visible radiation: optimization by response level method. Polyhedron 165, 188–196.

Talebi, S., Chaibakhsh, N., Moradi-Shoeili, Z., 2017. Application of nanoscale ZnS/TiO$_2$ composite for optimized photocatalytic decolorization of a textile dye. J. Appl. Res. Technol. 15 (4), 378–385.

Trindade, S.G., Federal, U., Maria, D.S., 2014. Synthesis of gold nanoparticles stabilised by ionic liquids. Relatorio Final de Bolsista – 23rd Programa Bolsas de Verao Do CNPEM 11.

Tshemese, Z., Khan, M.D., Mlowe, S., Revaprasadu, N., 2018. Synthesis and characterization of PbS nanoparticles in an ionic liquid using single and dual source precursors. Mater. Sci. Eng. B: Solid-State Mater. Adv. Technol. 227, 116–121, http://dx.doi.org/10.1016/j.mseb.2017.10.018.

Tzani, A., Koutsoukos, S., Koukouzelis, D., Detsi, A., 2017. Synthesis and characterization of silver nanoparticles using biodegradable protic ionic liquids. J. Mol. Liq. 243, 212–218, http://dx.doi.org/10.1016/j.molliq.2017.08.039.

Verma, D.K., Hasan, S.H., Banik, R.M., 2016. Photo-catalyzed and phyto-mediated rapid green synthesis of silver nanoparticles using herbal extract of *Salvinia molesta* and its antimicrobial efficacy. J. Photochem. Photobiol. B: Biol. 155, 51–59, http://dx.doi.org/10.1016/j.jphotobiol.2015.12.008.

Xu, Y., Wu, S., Li, X., Meng, H., Zhang, X., Wang, Z., Han, Y., 2017. Ag nanoparticle-functionalized ZnO micro-flowers for enhanced photodegradation of herbicide derivatives. Chem. Phys. Lett. 679, 119–126, http://dx.doi.org/10.1016/j.cplett.2017.04.091.

Yehya, A.H.S., Asif, M., Kaur, G., Hassan, L.E.A., Al-Suede, F.S.R., Abdul Majid, A.M.S., Oon, C.E., 2019. Toxicological studies of *Orthosiphon stamineus* (Misai Kucing) standardized ethanol extract in combination with gemcitabine in athymic nude mice model. J. Adv. Res. 15, 59–68, http://dx.doi.org/10.1016/j.jare.2018.05.006.

Zhang, Y., Han, C., Zhang, G., Dionysiou, D.D., Nadagouda, M.N., 2015a. PEG-assisted synthesis of crystal TiO$_2$ nanowires with high specific surface area for enhanced photocatalytic degradation of atrazine. Chem. Eng. J. 268, 170–179, http://dx.doi.org/10.1016/j.cej.2015.01.006.

Zhang, Y., Liu, P., Wu, H., 2015b. Development of high efficient visible light-driven N, S-codoped TiO$_2$ nanowires photocatalysts. Appl. Surf. Sci. 328, 335–343, http://dx.doi.org/10.1016/j.apsusc.2014.12.043.